Transition Metal Doping Investigation in TiO$_2$/CdS

6.1 Introduction

Several strategies have been employed to improve performance of Quantum Dot Sensitized Solar Cells [Tian and Cao, 2013]. These strategies normally focus on effective passivation of Quantum Dots and mesoporous electrode to reduce recombination and others strategies focuses on altering absorption window of quantum dot absorber as shown schematically in Figure 6.1. Specially core-shell design of Quantum Dots called as exciplex quantum dots have shown good photovoltaic properties in Quantum Dot Sensitized Solar Cells [Jiao, Shen, Mora-Sero, et al., 2015]. Alloyed QDs like CdTe$_{1-x}$Se$_x$ have also shown good performance [Pan et al., 2013]. Additional passivation schemes like ZnS [Néstor Guijarro et al., 2011] and SiO$_2$ passivation [Zhao et al., 2015] have shown comparatively reduced recombination. Ligand exchange also resulted in improvement efficiency of QDSSCs as shorter and more conducting ligand [Nestor Guijarro et al., 2009] also assist in conduction of electron that results in improvement of efficiency.
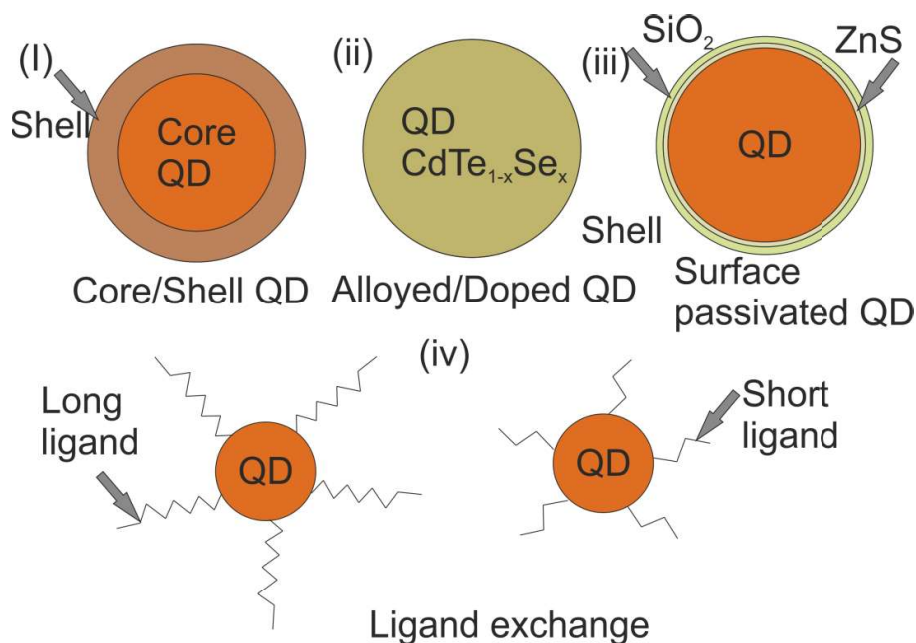

Figure: 6.1 Schematic representation of adopted strategies for improvement in QDSSC.

Transition metals like Mn have also been utilized to dope QDs and doping with transition metal doping has normally resulted in improvement in efficiency. Kamat et al. have investigated doping of Mn in Cadmium Sulfide QDs and showed good improvement in efficiency [Santra and Kamat, 2012]. They have associated this improvement in efficiency to the introduction of long living Mn transition ($^4T_1$-$^6T_1$) in between conduction band minima and

valance band maxima of CdS quantum dots. They also showed extended window of absorption for Mn doped CdS QDs. In 2015, Halder et al. used pre-synthesized Mn doped CdS QDs and identified Mn affected emission using temperature dependent photoluminance and conformed Mn substitutional doping using X-ray photoelectron spectroscopy [Halder and Bhattacharyya, 2015]. They predicted that in addition to substitutional Mn doing, there might be presence of Mn metal cluster, those may introduce recombination explaining reduction in photocurrent with higher Mn doping.

Table 6.1: The summarized different transition metal doped QDs based solar cells with respective short circuit current density (J_{sc}), open circuit voltage (V_{oc}) and efficiency with relative improvement without transition metal doped QDs solar cells.

QDs system	J_{sc} (mA/cm^2)	V_{oc} (Volt)	Efficiency (%)	Relative enhancement in photovoltaic response
Mn-d-CdS/CdSe [Santra and Kamat, 2012]	20.7	0.558	5.42	20% improvement in J_{sc}
Cu-d-PbS/CdS [Huang et al., 2013]	21	0.34	2.01	57% improvement in J_{sc}
CuInS$_2$/Mn-d-CdS [Luo et al., 2013]	19.29	0.58	5.38	10% improvement in J_{sc}
Mn-d-CdSe [Tian, Lv, et al., 2014]	19.15	0.58	6.33	30% improvement in J_{sc}
Co-d-CdS/CdSe [Firoozi et al., 2015]	16.62	0.45	3.16	26% improvement in J_{sc}
Mn-d-CdS [Halder and Bhattacharyya, 2015]	8.39	0.5	2.08	60% improvement in J_{sc}
CdS/CdSe/Mn-d-ZnSe [Gopi et al., 2015]	17.59	0.584	5.67	39% improvement in J_{sc}

However, these studies do not provide any insight towards the contribution of different energy levels introduced with these transition metal clusters and a rationale for selecting the suitable transition metal for an enhanced photovoltaic response.
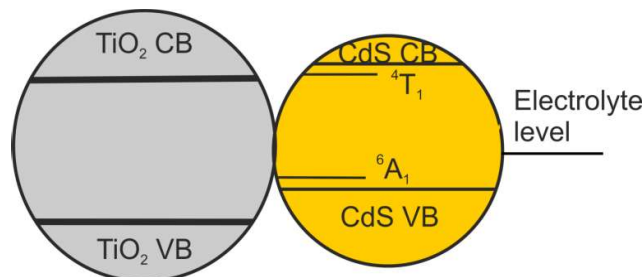

Figure: 6.2 Schematic diagram showing possible energy level in transition metal doped CdS system.

In this study, successive ionic layer adsorption and reaction (SILAR) method is used to sensitize mesoporous electrode with CdS QDs and for transition metal doping, respective transition metal precursor was dissolved in cadmium precursor. We selected transition metal based on their work function to explore effect of transition metal doping. The work function of Mn (-4.1 eV) is close to the conduction level (-4.0 to - 4.2 eV) of TiO_2 [Ha Thanh et al., 2014], and that of Fe (-4.5 eV) in between polysulfide electrolyte level and TiO_2 conduction level while Ni (-5.15 eV) lies close to the polysulfide electrolyte level (~ -5 eV) respectively with reference to vacuum [Halas, 2006], [Nieuwenhuys et al., 1974], [Hodes, 2012]. The different molar fractions of transition metal precursors are used to prepare the cation precursor for implementing different doping fractions. The sensitized electrodes are passivated with ZnS layer using SILAR to avoid back recombination [Néstor Guijarro et al., 2011] and their photovoltaic performance is evaluated under 100 mW/cm² Xenon lamp illumination.

6.2 Experimental Procedure

6.2.1 Mesoporous TiO₂/CdS Photoelectrode Preparation
FTO substrates were cleaned as explained in section 4.1.1.1. Cleaned FTO substrates were treated with $TiCl_4$ as described in section 4.1.1.2. Anatase TiO_2 powder was used to prepare paste for Dr. blade and mesoporous electrode were prepared and sintered as described in sections 4.1.2.2 and 4.1.2.3, respectively. TiO_2 mesoporous electrodes were sensitized with CdS QDs using SILAR as described in section 4.1.3.2. Transition metal precursors were dissolved along with cadmium precursor for transition metal doping. Manganese chloride ($MnCl_2$) was used for Mn, nickel chloride ($NiCl_2$) was used for Ni and iron chloride ($FeCl_2$) was used for Fe transition metal doping in CdS QDs. After sensitization with transition metal doped CdS QDs and pristine CdS QDs, these electrodes were passivated using ZnS coating as mentioned in section 4.1.3.3.

6.2.2 QDSSC Preparation and Characterization
Cu_2S counter electrode was utilized along with polysulfide electrolyte as mentioned in section 4.1.5.2 and 4.1.4, respectively. Structural characterization of zinc titanate nano powder and respective sensitized electrodes was done using XRD as described in section 4.2.1.1. Scanning electron microscopy was utilized in SE mode to image surface morphology of sintered electrode as described in section 4.2.1.2. Optical properties of mesoporous electrodes were calculated using diffuse reflectance accessory with Cary 4000 as described in section 4.2.2.2. QDSSCs are assembled with sensitized mesoporous photoelectrode and photovoltaic characterization and impedance characterization were done as described in section 4.2.3.1 and 4.2.3.2, respectively.

6.3 Results and Discussion

6.3.1 X-ray Diffraction Analysis
Figure 6.3 shows X-ray diffraction pattern for Mn (40 mole% of Cd) doped CdS sensitized mesoporous electrode. The pattern shows diffraction peaks corresponding to anatase TiO_2 (ICDD 03-065-5714) along with diffraction peaks of fluorine doped Tin oxide (FTO) substrate [Tachan et al., 2010]. No prominent peaks corresponding to CdS or Mn are found in the pattern. A diffraction peak at 26.6° 2 θ may correspond to CdS, where FTO diffraction peak is also present. This makes difficult to clearly distinguish CdS QD peak using XRD pattern. The FTO peaks are marked by square symbol and diffraction peaks corresponding to anatase TiO_2 are plotted in the bottom panel with ICDD database file 03-065-5714. No difference was

observed in XRD patterns for pristine CdS sensitized mesoporous and transition metal doped CdS sensitized mesoporous electrodes.
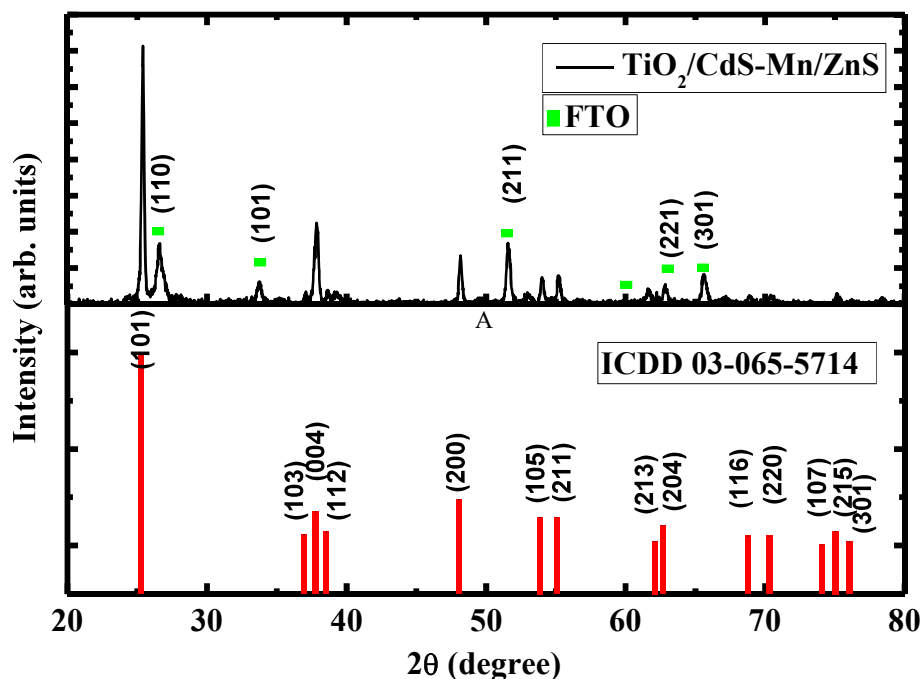

Figure: 6.3 X-ray diffraction for Mn doped CdS sensitized mesoporous electrode (upper panel) and anatase diffraction reference (lower panel).

6.3.2 Microstructure and Surface Roughness Analysis

Scanning electron microscopy images are shown in Figure 6.4 for sintered and sensitized mesoporous electrodes. Figure 6.4 (a) and (b) are low magnification images for sintered not sensitized and CdS QDs sensitized mesoporous TiO_2 electrodes. Both electrodes look quite different in surface morphology. Sintered electrode shows clean agglomerated nano particle network with pores while sensitized electrode shows film around sensitized electrode. For sensitized electrode, TiO_2 nano particles are not clearly visible.
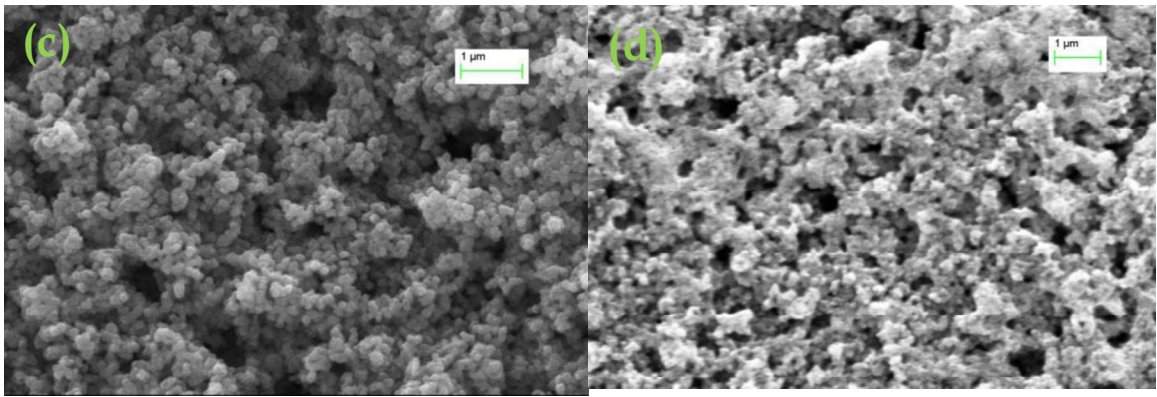

54
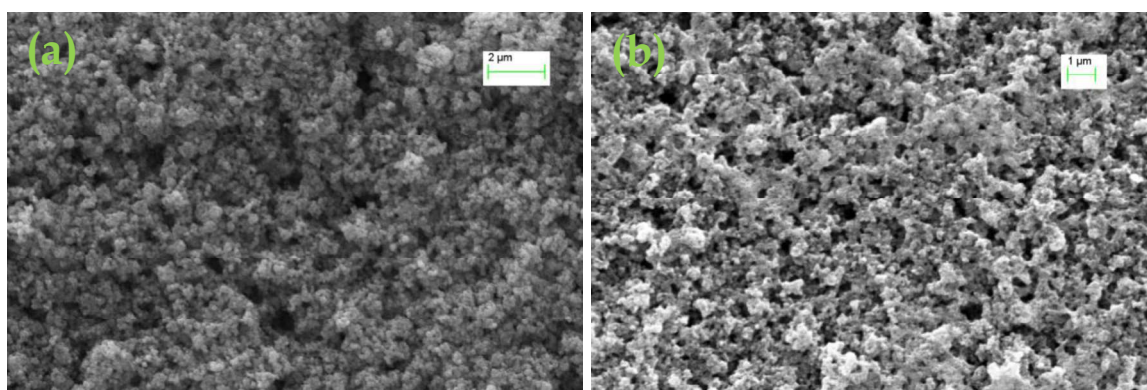
Figure: 6.4 Surface morphology for (a, c) non- sensitized electrode and (b, d) sensitized electrode.

Figure 6.4 (c) and (d) are higher magnification images for sintered non-sensitized and sensitized mesoporous TiO_2 electrodes. Interconnected nanoparticles are visible for sintered electrode while sensitized electrode slows agglomerated particles film around them and but pores are visible even in sensitized electrodes.

Topographical images for sintered non-sensitized and sensitized mesoporous electrodes are shown in Figure 6.5. Atomic force micrographs are collected in non-contact mode for 20 µm×20 µm, 5 µm×5 µm and 1 µm×1 µm scanning areas. XEI software supplied by Park system was used for analyzing topography images and to remove any surface artifacts.
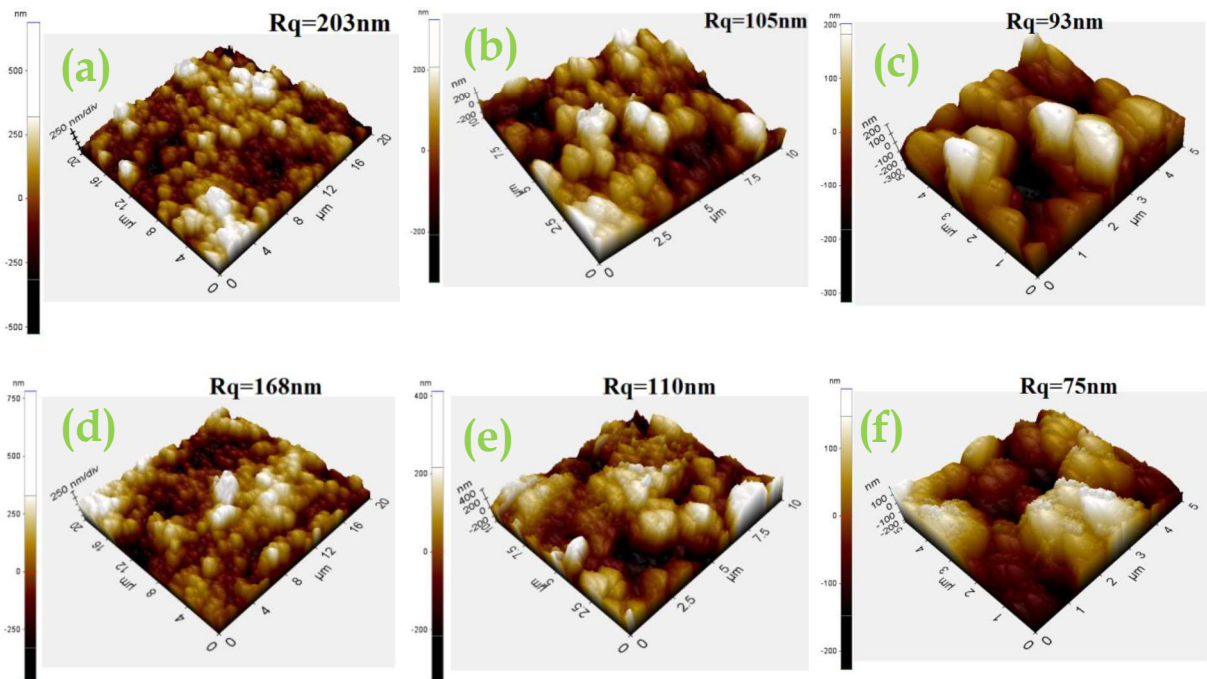

Figure: 6.5 Topography for (a, b, c) sintered and (d, e, f) sensitized electrode for different scanning area.

Surface topography of mesoporous electrode is shown in Figure 6.5, used for calculating rms values of surface roughness, which are marked in respective images. Figures 6.5 (a), 6.5 (b),

55

and 6.5 (c) show topography for sintered, non-sensitized electrodes and Figures 6.5 (d), 6.5(e), and 6.5 (f) for sensitized mesoporous electrodes. Island type topography is observed for mesoporous TiO$_2$ electrode and surface is highly rough. Even after sensitization, AFM images do not show drastic difference in surface roughness. For sensitized electrodes, we can see some smaller particle type topography on electrode for 5 μm × 5 μm scanning area in AFM topography as a signature of QDs growth, consistent with SEM images showing an agglomerated film.

6.3.3 Optical Properties Analysis

For optical characterization, diffuse reflectance measurements were made for mesoporous electrodes. Kubelka Munk transformation was utilized to convert diffuse reflectance to absorbance [Džimbeg-malčić et al., 2012]. Absorbance is shown in Figure 6.6 (a) for pristine CdS sensitized and Mn doped CdS sensitized mesoporous TiO$_2$ electrodes. We can clearly observe a 3.2 eV transition for TiO$_2$ and 2.4 eV transition for CdS QDs. Mn doping resulted in no significant change in absorption onset as evident from Figure 6.6 (a).
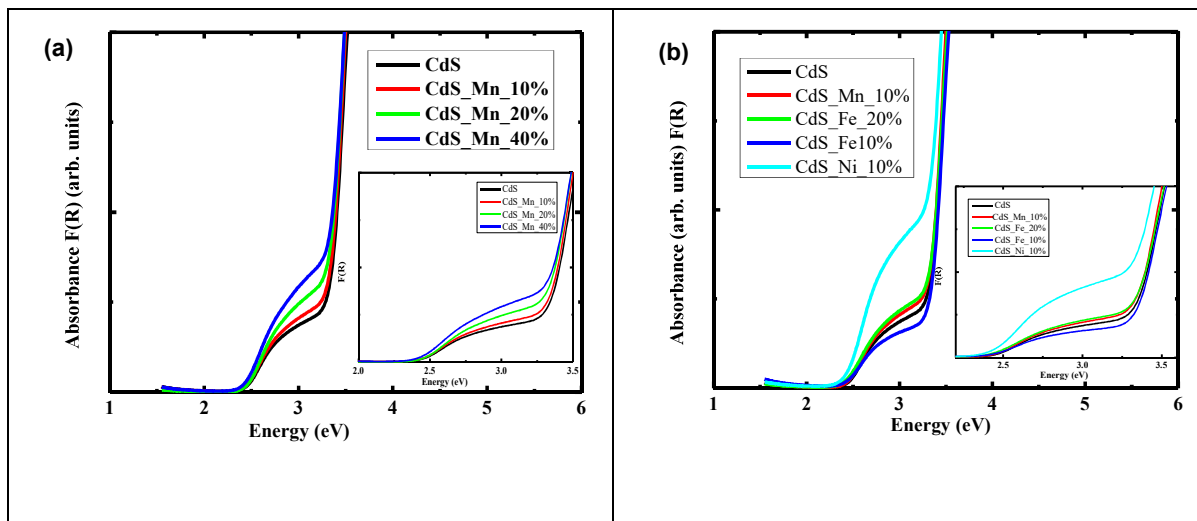

Figure: 6.6 Absorption of (a) Mn doped TiO$_2$/CdS electrode for different mole fraction and (b) different transition metal doped electrode.

Further, absorbance is shown in Figure 6.6 (b) for different mole fraction doping of different transition metals in CdS sensitized mesoporous electrode. In zoomed view, as shown in inset, we do not observe any significant change in absorption onset after transition metal doping. In earlier works summarized in section 6.1, change in absorption edge was shown with transition metal doping but any significant change in absorption onset was not observed in this study.

6.3.4 Photovoltaic Characterization of QDSSCs

Photovoltaic response were recorded and shown in Figure 6.7. We can see improvement in current for 10 mole% Mn doping, Figure 6.7 (a) which reduces for higher mole fraction doping. This behavior for Mn doped photoelectrodes is in agreement for earlier studies for Mn doping in CdS sensitized photoelectrode [T. Shen et al., 2016].
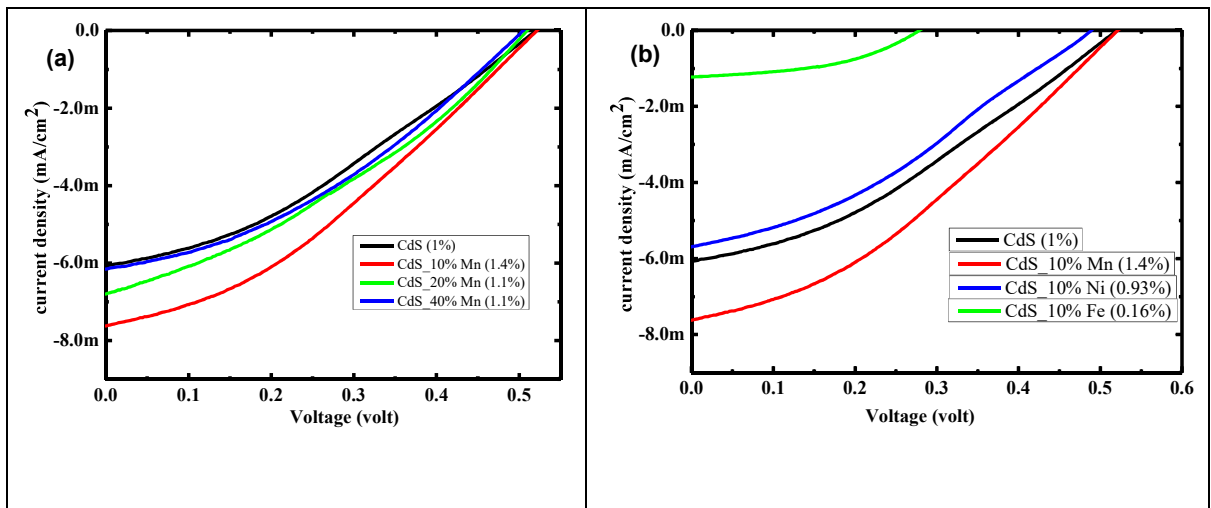
Figure: 6.7 current voltage characteristic for (a) Mn doped TiO₂/CdS electrode and (b) different transition metal doped TiO₂/CdS QDSSCs.

Further, photovoltaic response is shown in Figure 6.7(b) for different transition metal doped CdS QDs sensitized photoelectrode along with CdS QDs sensitized photoelectrode. For Ni transition metal doping, we see that there is some dip for higher voltage or "S" shaped curve that is normally associated with deep mono energetic surface states of TiO₂ [Mora-Seró et al., 2009]. It suggests that Ni doping introduces defect states those are close to polysulfide redox level. For Fe doped photoelectrode, we can see that photovoltaic response is not so good. It can be because of deep defect states those are getting introduced with Fe doping. With small amount doping of foreign element, localized donor or acceptor level are introduced. Even if doping is not substitutional, localized energy level get introduced due to presence of metal cluster [Sato, 1998]. It is expected that these level are getting introduced close to Fermi level of transition metal. The different QDSSC performance parameters were extracted from current – voltage characteristic and they are summarized in table 6.2.

Table 6.2: The photovoltaic device parameters for different TM doped photoelectrodes

S. No.	Electrode Specification	J_{sc} (mA/cm²)	V_{oc} (Volt)	FF	Efficiency (%)
1	CdS pure	4.98+/-0.79	0.5+/-0.03	0.43+/-0.08	1.07+/-0.3
2	Mn (10 mole%)	6.68+/-0.9	0.52+/-0.01	0.36+/-0.02	1.21+/-0.13
3	Mn (20 mole%)	4.85+/-1.3	0.49+/-0.16	0.34+/-0.02	0.8+/-0.2
4	Mn (40 mole%)	5.18+/-0.8	0.51+/-0.01	0.36+/-0.01	0.95+/-0.14
5	Ni (10 mole%)	4+/-1.22	0.48+/-0.01	0.35+/-0.02	0.67+/-0.18
6	Fe (10 mole%)	1.1+/-0.1	0.281+/-0.01	0.44+/-0.02	0.14+/-0.02

Impedance spectroscopy measurements were made on QDSSCs under dark from 100 KHz - 0.1 Hz frequency range as described in section 4.2.3.2. Nyquist plots and Bode plots for different QDSSCs for different photoelectrodes are shown in Figure 6.8.
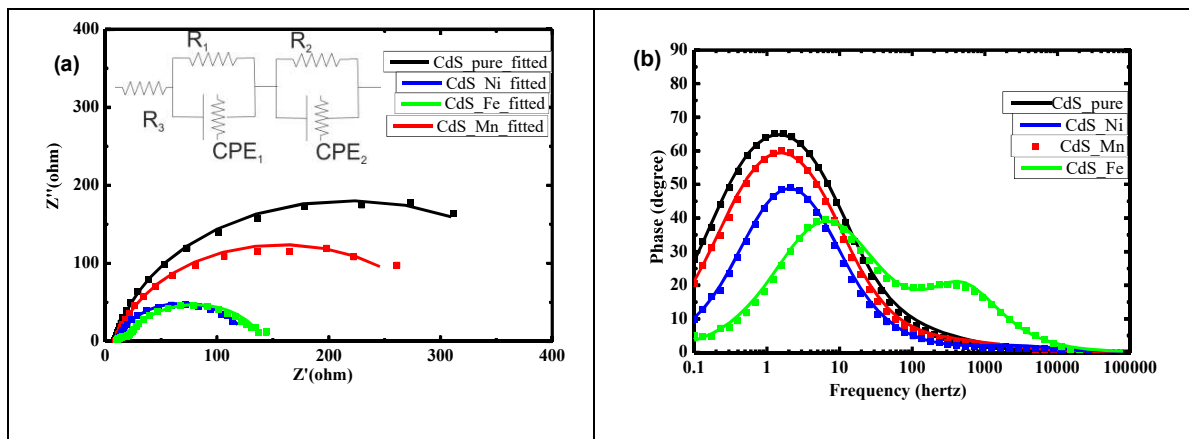

Figure: 6.8 (a) Nyquist plot and fitted Impedance spectra for TM doped QDSSCs and (b) bode plots for TM doped QDSSCs.

Impedance data was fitted using equivalent circuit model, shown as an inset in Figure 6.8 (a), and as described in section 4.2.3.2. The different device parameters are extracted from fitting and are summarized in Table 6.3. Figure 6.8 (a) shows lower recombination resistance for Fe doped photoelectrode with Ni and Fe. Even for Mn doped photoelectrode, recombination resistance has reduced but we see improvements in photovoltaic performance. All photoelectrodes showed similar interfacial resistance at counter electrode except for Fe doped photoelectrode. The interfacial resistance at counter electrode may increase due to introduction of possible mid-gap states.

Table 6.3: Extracted equivalent circuit parameters from impedance measurements for different transition metal doped and un-doped photoelectrode based QDSSCS

Photoelectrode	R_s(ohm)	R_{rec} (ohm)	C_{rec}(F)	R_{ce}(ohm)	C_{ce}(F)
CdS_pure	8.45	418	2.1m	1.38	0.691m
CdS_Mn	9.84	295	2.2m	1.18	0.224
CdS_Ni	10.07	115	2.4m	0.976	0.057
CdS_Fe	10	122	0.607m	9.44	0.044

Bode plots for photoelectrodes are shown in Figure 6.8(b). Carrier lifetimes were calculated from Bode plots using $carrier\ lifetime = \frac{1}{2\pi f_{max}}$ equation [Kern et al., 2002].

Calculated carrier lifetimes are summarized in Figure 6.9 (a). It is shown that carrier lifetime for CdS sensitized photoelectrode and Mn doped CdS sensitized photoelectrode is similar. However it was observed that for Mn doped photoelectrode recombination resistance was lower which may be due to introduction of Mn states resulting in improved transportation of injected photoexcited carriers.
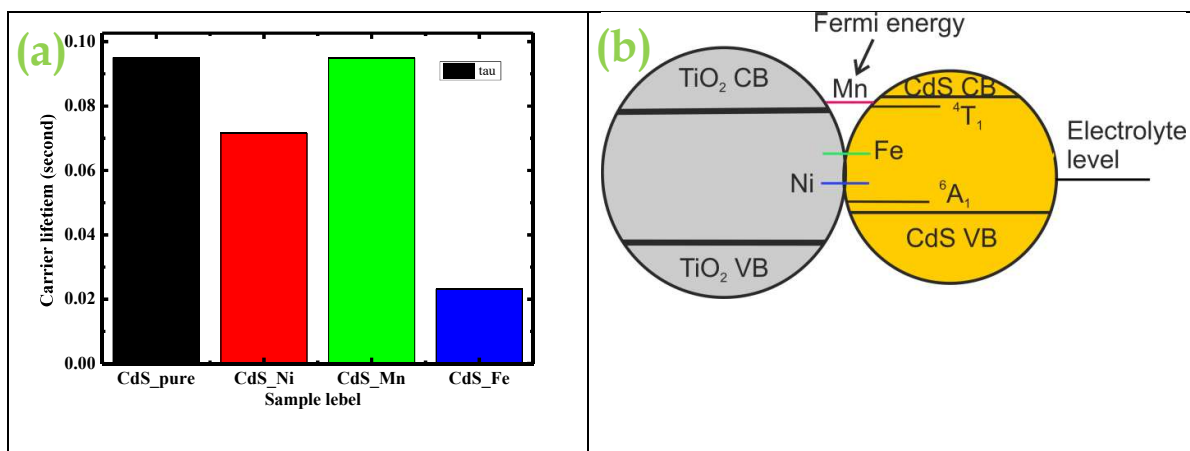

Figure: 6.9 (a) Carrier lifetime for transition metal doped QDSSCs and (b) schematic diagram of introduced energy level diagram indicating Fermi energy of transition metal dopants.

Figure 6.9 (b) shows schematic representation of band level alignment in QDSSCs and Fermi level of dopants. Mn Fermi level is close to TiO_2 conduction band minima and CdS conduction level, showing improved photovoltaic response. Thus, if energy levels are introduced close to this Fermi energy, carrier transportation may improve. Ni Fermi energy is close to polysulfide electrolyte, suggesting that if energy levels are introduced at this energy, it can serve as deep energetic states and will results in "S" shaped curve as already observed in section 6.3.4. Fe Fermi energy lies in mid of electron transport material conduction band minima and red-ox level of polysulfide electrolyte, causing introduction of energy levels close to Fe Fermi energy. These states will act as mid band states and lead to enhanced recombination, causing poor photovoltaic performance. Earlier, J. Wu. et al. studied native defects and transition metal dopings in CdS using density functional theory and observed that the transition metal doping in Cd rich condition will produce interstitial doping in CdS. They calculated density of states in such system using spin polarized hybrid DFT calculation by making use of Heyd-Scuseria-Ernzerhof (HSE06) method. They used screened hybrid functional with 30 % Hartree Fock Exchange. Transition metal Mn introduced density of states within CdS conduction band, whereas Ni interstitial doping resulted in dopant density of states of about 1 eV lower to CdS conduction band minima and close to polysulfide redox potential. The iron interstitial doping resulted in defect density of states close to CdS conduction band minima i.e. in between conduction band minima of TiO_2 and redox level of polysulfide electrolyte. These results are in agreement with our proposed hypothesis of introduction of energy level close to Fermi energy of transition metal dopant, dominating the photovoltaic response, as discussed earlier [Wu et al., 2011].

6.4 Concluding Remarks

In this study, transition metals with different work function or Fermi energy are doped in CdS sensitized photoelectrodes using SILAR. No improvement in absorption window was observed using diffuse reflectance measurement but effect on photovoltaic performance was observed for Mn doping among different dopants. The effect of dopants on photovoltaic performance was correlated with the introduction of additional energy levels close to Fermi energy of dopants. We concluded that doping with a transition metal whose work function is close to conduction band of electron transport material, may be beneficial for photovoltaic properties. In contrast, if work function lies in between conduction band level of electron transport material and red-ox level of polysulfide electrolyte, it may hamper photovoltaic performance.

...